energy&fuels

pubs.acs.org/EF Article

Solar Redox Cycling of Ceria Structures Based on Fiber Boards, Foams, and Biomimetic Cork-Derived Ecoceramics for Two-Step Thermochemical H_2O and CO_2 Splitting

Anita Haeussler, Stéphane Abanades,* Fernando A. Costa Oliveira, M. Alexandra Barreiros, A. P. F. Caetano, Rui M. Novais, and Robert C. Pullar

Cite This: *Energy Fuels* 2020, 34, 9037−9049 Read Online

ACCESS | Metrics & More | Article Recommendations

ABSTRACT: Solar thermochemical conversion of H_2O and captured CO_2 is considered for the production of high-value solar fuels and CO_2 valorization, using nonstoichiometric oxygen-exchange redox materials. This work aims to compare the thermochemical cycle performance of different ceria structures, including biomimetic cork-templated ceria (CTCe), ceria foams (CeF), and ceria bulk fiber boards (CeFB), to study the effect of the morphology on fuel production from two-step H_2O and CO_2 splitting via solar redox cycling. The considered materials underwent thermochemical cycles in a directly irradiated solar reactor under various operating conditions. Typically, a thermal reduction at 1400 °C under Ar at atmospheric pressure, using concentrated solar energy, was carried out followed by an oxidation step with H_2O or CO_2 between 800 and 1050 °C. The comparison of the fuel production rate and yield from the reactive materials highlighted the importance of the material thermal stability during cycling. CTCe and CeF showed good O_2 and fuel production stability over repeated cycles, while CeFB exhibited a decrease of the production because of sintering and thermal gradient due to its low thermal conductivity. Biomimetic CTCe showed a higher fuel production rate compared to the other investigated materials, explained by the favorable microstructure of the cork-based ceramic. The morphology obtained from the cork structure led to the improvement of the redox activity, demonstrating the relevance of studying this material for thermochemical H_2O and CO_2 splitting cycles. In addition, the impact of the operating conditions was investigated. A decrease of the starting oxidation temperature, an increase of the CO_2 molar fraction (lower CO/CO_2 ratio), or a high total gas flow rate favoring gas product dilution had a beneficial impact on the CO (or H_2) production rate.

1. INTRODUCTION

The limitation of the global warming impact requires the substitution of fossil energies by low-carbon energy. Solar-driven technologies offer a sustainable solution to replace fossil fuels and to limit climate change, owing to the unlimited and widespread availability of the solar resource.[1] The major issue of solar energy, namely, intermittence, is discordant with the actual energy grid that requires constant energy input. An answer can arise from the conversion of the solar energy to long-term storable chemical fuels.[2,3] Indeed, this route presents advantages by producing dispatchable solar fuels which are usable on demand and transportable, overcoming the intermittence issue.[4] Thermochemical cycles permit solar energy conversion into chemical energy, with entire solar spectrum utilization and with a high theoretical efficiency due to direct solar-to-fuel conversion, without requiring intermediate low-efficiency electricity production or the use of precious metal catalysts. Solar thermochemical approaches to split CO_2 and H_2O inherently operate at high temperatures and provide an attractive path to solar fuel production with higher energy conversion efficiencies than photochemical or electrochemical methods. Solar-driven H_2O- and CO_2-splitting using redox materials constitutes an attractive option for massive synthetic fuel production, avoiding greenhouse gas emission and allowing complete recycling of chemical intermediates. The two-step process first consists of the thermal reduction of a metal oxide, while oxygen is released by the creation of oxygen vacancies in the oxide lattice (reaction 1). In a second step, the reactive material is reoxidized with either CO_2 or H_2O, resulting in fuel production (reaction 2).

$$M_xO_y \rightarrow M_xO_{y-\delta} + \frac{\delta}{2}O_2 \quad (1)$$

$$M_xO_{y-\delta} + \delta CO_2(H_2O) \rightarrow M_xO_y + \delta CO(H_2) \quad (2)$$

The possible generation of both H_2 and CO (syngas) with the same material allows the production of liquid fuels, commonly called synthetic fuels, from low energy content sources (namely H_2O and CO_2). Indeed, syngas with appropriate H_2 and CO proportions can be converted into various hydrocarbon fuels via the Fischer−Tropsch process.[5] Ceria is currently designated as the benchmark material to perform

Received: April 16, 2020
Revised: June 4, 2020
Published: June 4, 2020

Downloaded via LABOR NACIONAL ENERGIA GEOLOGIA LNEG 20400 on August 13, 2020 at 14:45:28 (UTC).
See https://pubs.acs.org/sharingguidelines for options on how to legitimately share published articles.

ACS Publications © 2020 American Chemical Society

https://dx.doi.org/10.1021/acs.energyfuels.0c01240
Energy Fuels 2020, 34, 9037−9049

Table 1. Summary of the Main Experimental Studies, with the Key Operating Conditions and Outcomes, for Ceria Materials in Thermochemical Cycles

references	materials	facility used	operating conditions	oxidant	fuel production rate and yield
Furler et al.[33]	ceria felt	solar simulator	T_{red} = 1460−1647 °C	CO_2/H_2O	1.9 mL/min/g
			T_{ox} < 927 °C		262 μmol/g
Furler et al.[35]	ceria foam	solar simulator	T_{red} = 1420 °C	CO_2	0.127 mL/min/g
			T_{ox} < 1000 °C		65 μmol/g
Costa Olivera et al.[43]	ceria foam	solar furnace	T_{red} = 1400 °C	H_2O	0.6−0.8 mL/min/g
			T_{ox} = 1050−850 °C		115 μmol/g
Costa Olivera et al.[43]	cork templated ceria granules	solar furnace	T_{red} = 1400 °C	H_2O	1−1.4 mL/min/g
			T_{ox} = 1050−850 °C		133 μmol/g
Chueh et al.[44]	porous monolithic ceria	solar simulator	T_{red} = 1420−1640 °C	CO_2	4.6 mL/min/g
			T_{ox} < 900 °C		192 μmol/g
Cho et al.[45]	inert zirconia foam with CeO_2 coating	solar furnace	T_{red} = 1400−1600 °C	H_2O	116 μmol/g
			T_{ox} = 1100−900 °C		
Marxer et al.[46]	dual scale porosity ceria foam	solar simulator	T_{red} = 1450−1500 °C	CO_2	1.2 mL/min/g
			P_{red} = 10 mbar		276 μmol/g
			T_{ox} = 700−1000 °C		
Haeussler et al.[47,48]	microstructured ceria foam	solar furnace	T_{red} = 1400 °C	CO_2/H_2O	8.36 mL/min/g
			T_{ox} = 1008−796 °C		254 μmol/g
Gladen and Davidson[49]	commercial fibrous ceria particles	electric furnace	T_{red} = 1500 °C	CO_2	8.4 mL/min/g
			T_{ox} = 800 °C		51 μmol/g

thermochemical cycles, given its ability to maintain its crystallographic structure over a large range of nonstoichiometry, together with its thermodynamically favorable oxidation and high oxygen storage capacity, which makes it suitable to perform thermochemical cycles with high performance stability. Numerous studies have been devoted to ceria,[6−14] and the addition of dopants[15−31] to enhance its redox performance. However, ceria redox activity depends on the reduction temperature and oxygen partial pressure applied during the high-temperature step, which is generally limited to ∼1500 °C due to undesired oversintering and ceria sublimation. Doping ceria with metallic cations generally showed a beneficial impact on the maximum reduction extent reached, but with an adverse effect on the reoxidation step. The reduction step is affected by the diffusion length for lattice oxygen transfer, while the oxidation reaction largely depends on the porous structure and specific surface area of the material, since it is a surface-controlled solid/gas reaction. These two properties are impacted by the reactive material microstructure,[32] which is thus a key parameter for enhancing the thermochemical performance.

Among a variety of potential candidates, ceria fiber felt was first investigated to perform two-step thermochemical cycles in solar reactors, because the use of such designed 2D or 3D morphologies enhances fuel production rates. Furler et al.[33] reached a nonstoichiometry extent δ of 0.044 with a commercial ceria felt during the reduction step at 1650 °C. They obtained a syngas production of 5.88 mL/g with a solar-to-fuel energy conversion efficiency of 0.15%. The heat transfer limitation induced by low thermal conductivity of the ceria felt was the main reason for the low efficiency.[33] To overcome the poor thermal conductivity of the felt, reticulated porous ceramics (RPC), such as foams, have been explored to perform thermochemical cycles. To prepare reticulated porous ceramic (RPC) foams, one of the most commonly employed methods is the replication technique.[34] Furler et al.[35] obtained a nonstoichiometry extent up to 0.042 at a reduction temperature in the range of 1400−1600 °C with a ceria RPC foam. The achieved solar-to-fuel energy conversion efficiency reached 1.73%, namely, a 4-fold increase compared with ceria felt. However, due to the low specific surface area, the peak fuel production rate was low. Dual-scale porosity RPC foams, combining millimeter-pore size with micrometer-pore size within the foam struts, were developed to favor the oxidation step, which provided a faster fuel production rate with a higher fuel yield in comparison with single-scale foam.[36] Another type of morphology investigated in the literature consists of three-dimensionally ordered macroporous (3-DOM) structures that enhance fuel production rates. Venstrom et al.[37−39] obtained an inverse replica of a face-centered cubic close-packed array, forming a 3-DOM structure of ceria. The 3-DOM object of ceria as synthesized exhibits a specific surface area (SSA) of 30 m^2/g, which decreased to 10 m^2/g after the thermochemical cycles. With 3DOM material, the peak production rate was enhanced (by 260%) in comparison with low porosity ceria material. The improvement of the oxidation kinetic was attributed to the high SSA and the interconnected pore structure of the 3DOM material.[37] Recently, ecoceramics were developed for being applied in solar reactors to perform thermochemical cycles.[40,41] Ecoceramics use natural sustainable materials as templates to produce biomimetic ceramics, offering the advantages of being cost-effective and eco-friendly.[42] They also create 3DOM structures, based on the natural cellular morphology of the template material, usually a wood. Pine wood templated ceria permitted a 5−6-fold increase of the oxidation rate after a reduction at 1400 °C compared with nonporous ceria, but the microstructure was not retained after thermal treatment at 1500 °C.[40] Another study highlighted a 2-fold increase of the CO production rate in cork-templated ceria compared with RPC ceria foam. The mean cell size of the biomimetic material was one order of magnitude smaller than that of the ceria foam, providing a higher available surface for the oxidation reaction.[41] Table 1 summarizes different key studies with operating conditions and associated fuel production, highlighting the influence of the selected ceria structure on both fuel production rates and yields.

https://dx.doi.org/10.1021/acs.energyfuels.0c01240
Energy Fuels 2020, 34, 9037−9049

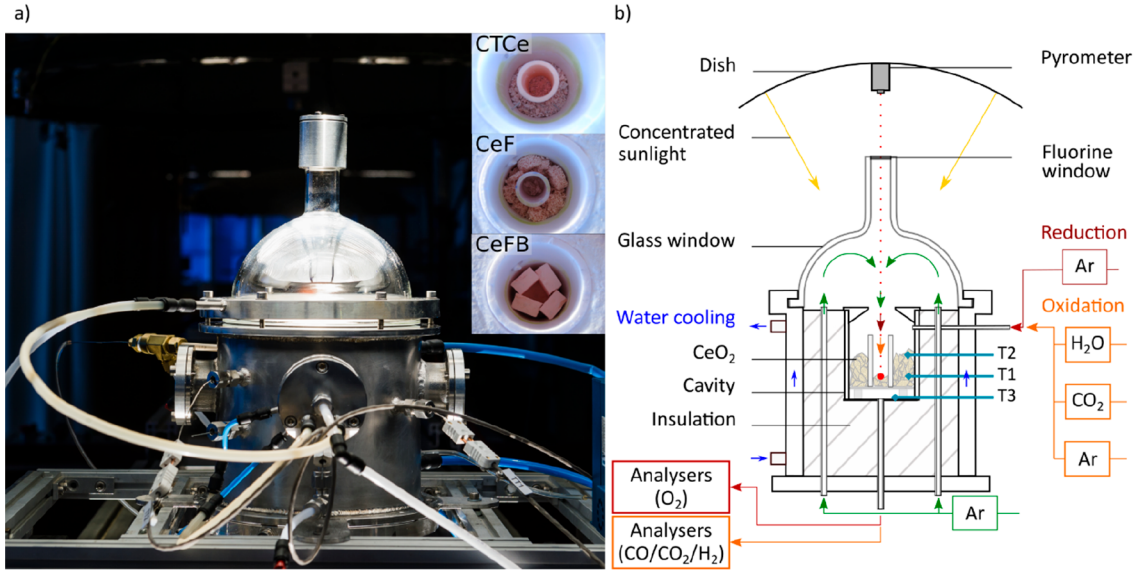

Figure 1. (a) Photograph of the solar reactor. Image insets on the right show CTCe, CeF, and CeFB (from top to bottom) inside the alumina cavity. (b) Schematic illustration of the solar reactor. Red arrows represent the gas flow during the reduction step; orange arrows, the gas flow during the oxidation step; green arrows, the Ar flow injected during both steps to protect the glass window and sweep the cavity; and blue arrows the water cooling.

This study aims to compare the thermochemical performance in a solar reactor of three structured materials, in order to highlight the impact of the material morphology on redox activity. Accordingly, ceria-based materials with different morphologies have been selected to compare their ability for two-step thermochemical H_2O and CO_2 splitting, namely, biomimetic cork-templated ceria, ceria RPC foam, and ceria fibers, using a specifically designed solar reactor heated by real high-flux concentrated solar radiation.

2. EXPERIMENTAL SETUP AND METHODS

2.1. Materials Synthesis and Characterization. The considered materials were biomimetic cork-templated ceria, ceria foam, and ceria fibers, abbreviated as CTCe, CeF, and CeFB, respectively.

CeFB fiber boards (>99% purity) were supplied from Zircar Zirconia Inc. USA (density: 1.153 kg/m^3). The other ceria-based materials, namely, cork-derived ecoceramic granules and polymer replicated foams, were synthesized at the University of Aveiro and LNEG, respectively. CTCe was synthesized according to a procedure previously detailed in ref 50. In brief, cork granules were heat treated in N_2 at 900 °C for 30 min to form carbon templates, then infiltrated with cerium nitrate solution ($Ce(NO_3)_3{\cdot}6H_2O$, 99%, Sigma-Aldrich). After the infiltration/drying step, the materials were heated in air to 1600 °C for 30 min to remove the carbon, forming a pure ceria ceramic with the 3DOM structure of cork, consisting of hexagonal cells ∼20 μm in diameter. Polymeric templated ceria foams (CeF) of cylindrical shape (25 mm in diameter and 12 mm height) were produced using the replication method. An aqueous slurry of cerium oxide powder (99.9% purity, average particle size of 1 μm, slurry content of 40 vol %) was prepared with 0.8 wt % anionic polyelectrolyte dispersant (Dolapix CE64, Zschimmer and Schwarz, F.R. Germany) and the addition of 5 wt % polyvinyl alcohol (PVA, Riedel-de-Haën, F.R. Germany) for structure stabilization in order to prevent the collapse of the foam structure during polymer removal. The slurry was then used to impregnate open-cell polyurethane (PU) foams (grade 20DB, manufactured by Flexipol – Espumas Sintéticas S.A., Portugal). The mean cell size of the PU foams was determined to be ∼700 μm (36 ppi) by using image analysis. After drying, the samples were heated at 1 °C min^{-1} to 500 °C for 1 h and subsequently sintered at 1450 °C for 30 min.

The materials' redox activity was determined by thermogravimetric analysis (TGA, Setaram Setsys Evo 1750) in controlled atmospheres. The sample (about 105 to 125 mg) was placed in a Pt crucible and submitted to two thermochemical cycles with the reduction step carried out at 1400 °C (heating rate of 20 °C min^{-1}), held for 45 min, in flowing Ar at 20 mL min^{-1} (99.999% purity), and the oxidation step at 1050 °C, held for 60 min, in a flowing CO_2 stream mixed with Ar (total flow rate of 20 mL min^{-1}, 50% CO_2 in Ar). The sample mass loss during reduction (due to oxygen release) and gain during oxidation (due to oxygen replenishment from CO_2 gas to produce CO) were measured to determine the O_2 and CO production yields.

The morphology of the materials before and after cycling was studied by scanning electron microscopy (SEM). Samples were mounted on stubs with carbon tape, and then imaged on a Philips XL30 FEG electron microscope using an acceleration voltage of 3–10 kV. The true density of the ceria was determined using an AccuPyc 1330 Helium pycnometer (Micromeritics Int. Corp., USA). Nitrogen adsorption measurements were carried out at −196 °C using a Micromeritics ASAP 2020. Before each measurement, the samples were degassed at 4 × 10^{-3} mbar and 300 °C for 12 h.

2.2. Solar Reactor Configuration. Figure 1 represents the schematic diagram of the monolithic solar reactor heated by concentrated solar radiation.[47] The solar experimental setup is composed of an alumina cylindrical cavity (80 mm height and 50 mm inside diameter, volume of 0.15 L) that is closed with an alumina top cover (with 18 mm aperture). The high-flux solar radiation directly irradiates the cavity through a hemispherical Pyrex glass window. The cavity receiver was insulated with a fibrous layer of porous alumino-silicate. For the cork-templated ceria granules and ceria foam materials, an alumina confiner tube was placed at the cavity center to position and keep the main part of the reactive material around the tube in the annular region, while the remaining portion of reactive material was placed at the tube bottom center, so as to permit a good and uniform heating of the whole reactant owing to radiation exchange inside the central tube cavity. In the case of the ceria fibers, four boards were cut and placed vertically in the cavity without the alumina tube. The external reactor stainless-steel shell is water-cooled. The concentrating system consists of a 2-m-diameter parabolic dish (1.5 kW nominal thermal power for DNI of 1000 W/m^2) coupled with a sun-tracking heliostat.

Three B-type thermocouples, along with a solar-blind pyrometer pointing in the cavity center, were used to monitor the temperature in

https://dx.doi.org/10.1021/acs.energyfuels.0c01240
Energy Fuels 2020, 34, 9037–9049

the solar reactor at various locations, as shown in Figure 1. The pressure in the cavity and in the gas flow inputs was measured using pressure sensors. The different gas flows were controlled with mass-flow controllers (MFC, Brooks Instruments model SLA5850S). Argon was injected from the reactor bottom toward the glass window to maintain an inert atmosphere and protect the window. Then, the gas entered downward in the cavity through the cover aperture. The oxidant gas was injected directly into the cavity from the lateral gas entrance, to permit a rapid switch of the gas flow between reduction and oxidation steps. During the reduction step, pure Ar (99.999% purity with $[O_2]$ < 2 ppm) was injected, whereas a mixture of Ar/oxidant (either pure deionized water or CO_2 with 99.995% purity) was injected during the oxidation step. In the case of water splitting, a liquid mass flow controller (range 0−60 g/h, accuracy ±1% of full scale) was used to inject water through an alumina capillary placed inside the lateral entrance (water was vaporized when exiting the tube and then carried by the Ar flow via the lateral inlet port). During the reduction step, the reactor was heated (up to ∼1400 °C) with concentrated solar radiation, and the heating rate was controlled by an intermediate shutter placed between the heliostat and the solar dish concentrator. The shutter opening was gradually increased to avoid thermal shocks, and the solar power input was thus controlled to keep the heating rate at ∼20−30 °C/min. During this stage, the reactor was swept with 1.2 L/min of Ar, while the oxygen released by the reactive material was continuously measured using a trace O_2 electrochemical analyzer (Systech, range from 0.1 ppm to 1%, precision ±2% of reading). The O_2 concentration typically increased during heating, until reaching a maximum close to the temperature set point for reduction. When the O_2 production dropped below 500 ppm during the temperature dwell, the shutter was then totally closed to cool down the system and the O_2 rapidly returned to below ∼20 ppm, so that the reduction step was considered complete. Following this, the reactor was cooled down to the oxidation temperature (∼1000 °C) by cutting the solar energy input. Once the targeted temperature was reached, the oxidant gas (CO_2 or H_2O) was injected into the reactor, and the resulting fuel produced was measured with a specific gas analyzer. Oxidation was performed under nonisothermal conditions, without any solar power input upon free cooling, in view of the fact that the continuous temperature decrease favors the oxidation thermodynamics. In the case of CO_2 splitting, the CO and CO_2 concentrations at the reactor output were measured by nondispersive infrared sensors (MGA3000, full scale: 0−30% for CO, 0−100% for CO_2, precision ±1% of full scale). For water splitting, a bubbler filled with ice/liquid water mix and a gas dryer were placed at the gas outlet to trap unreacted steam and protect the analyzer placed downstream. The hydrogen concentration peak evolution was measured with a devoted analyzer using a thermal conductivity detector (catharometer for Ar/H_2 binary mixture; scale, 0−10%; precision, ±1% of full scale). When the fuel production rate approached nearly zero, the oxidant injection was stopped to perform the next thermochemical cycle. The different amounts of gas produced were calculated by integrating the gas production rates over time. An automated data acquisition system (Beckhoff) recorded the various parameters (temperatures, pressures, gas flow rates, and gas concentrations) every second.

3. RESULTS AND DISCUSSION

Thermogravimetric analysis (TGA) was first performed to study the redox activity of the reactive materials before their integration and performance evaluation in the solar reactor. The amounts of O_2 and CO produced in the TGA are in agreement with the typical values reported for ceria powder.[15,51] The O_2 and CO amounts produced in the TGA are comparable for the three investigated materials, in the range of 47−51 μmol/g and 83−99 μmol/g, respectively (Figure 2 and Table 2). The reoxidation extent is above 84% in all the cases.

To study the redox activity of the investigated materials in the solar reactor, each material was submitted to consecutive

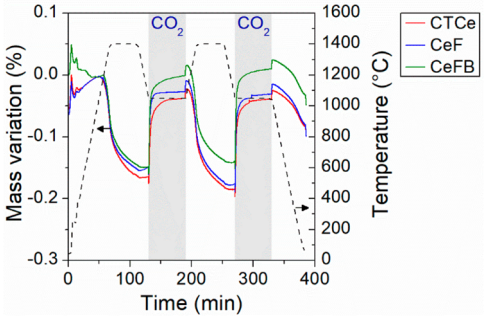

Figure 2. Reduction and reoxidation profiles of CeFB, CeF, and CTCe determined by TGA along with the temperature profile (dashed line).

thermochemical cycles with different operating parameters (Figure 3). The goal of the solar experiments and redox cycling of different ceria structures in a solar reactor was to demonstrate the solar process reliability, controllability and suitability for operation under real high flux solar irradiation, thus under representative conditions found in a real process. The most relevant parameters were also investigated with the aim of optimizing the thermochemical redox performance. Changing of the testing parameters such as inlet gas flow rates/compositions is also needed to show the performance sensitivity to the process conditions. Such experiments also demonstrate the materials stability and are useful to identify which ceria structure is the most suitable for operation in the solar reactor under real cycling conditions. The CTCe material was subjected to sixteen cycles, corresponding to 20 h of successive cycles under continuous on-sun operation (tests performed upon four consecutive days), whereas CeF and CeFB each underwent seven cycles, equivalent to ∼10 h (achieved during two consecutive days) of continuous on-sun operation (i.e., solar reactor continually heated with highly concentrated sunlight except during interruptions at night periods). The operating conditions used for each cycle are summarized in Table 3. The highest peak fuel production rate obtained in this study reached 3.1 mL/g/min using CTCe (with reduction at ∼1400 °C under atmospheric pressure). In comparison, other studies[46,52,53] achieved a peak production rate of 1.2 mL/g/min using ceria foams cycled with more favorable operating conditions (reduction step at 1500 °C under 10 mbar). Moreover, a previous study[41] using cork-templated ceria granules in a tubular packed-bed solar reactor reported a CO peak production rate of 1.9 mL/min/g under similar conditions (reduction step at ∼1400 °C and atmospheric pressure). Clearly, an improvement of the peak fuel production rate was obtained in comparison with previous reported data, showing the relevance of the studied materials integrated within the developed solar reactor.

For CTCe and CeF, the O_2 and CO amounts produced in the solar reactor are 28% and 36% higher than those obtained in TGA, caused by the temperature gradient in the cavity (meaning higher temperatures in the upper part of the cavity, as suggested by T2 and $T_{pyrometer}$ being higher than T1). For CeFB, the O_2 and CO production yields obtained in the solar reactor are three times higher than those obtained in TGA. In order to further explain the superior redox activity of CeFB over the other tested materials, special attention must be paid to the temperature profile along the height of the material. The high fuel productivity of CeFB can be explained by the high

https://dx.doi.org/10.1021/acs.energyfuels.0c01240
Energy Fuels 2020, 34, 9037−9049

Table 2. O_2 and CO Produced during TGA along with the Nonstoichiometry Extents (δ), Reoxidation Yields, and Peak Production Rates

cycle #	O_2 produced (μmol/g)	δ mol/mol	peak O_2 production rate (mL/min/g)	CO produced (μmol/g)	reoxidation yield	peak CO production rate (mL/min/g)
			CTCe			
1	51	0.018	0.084	86	84%	0.652
2	51	0.018	0.079	98	96%	0.843
			CeF			
1	47	0.016	0.087	83	88%	0.908
2	53	0.018	0.087	99	93%	1.042
			CeFB			
1	47	0.016	0.086	99	100%	1.021
2	49	0.017	0.086	99	100%	1.044

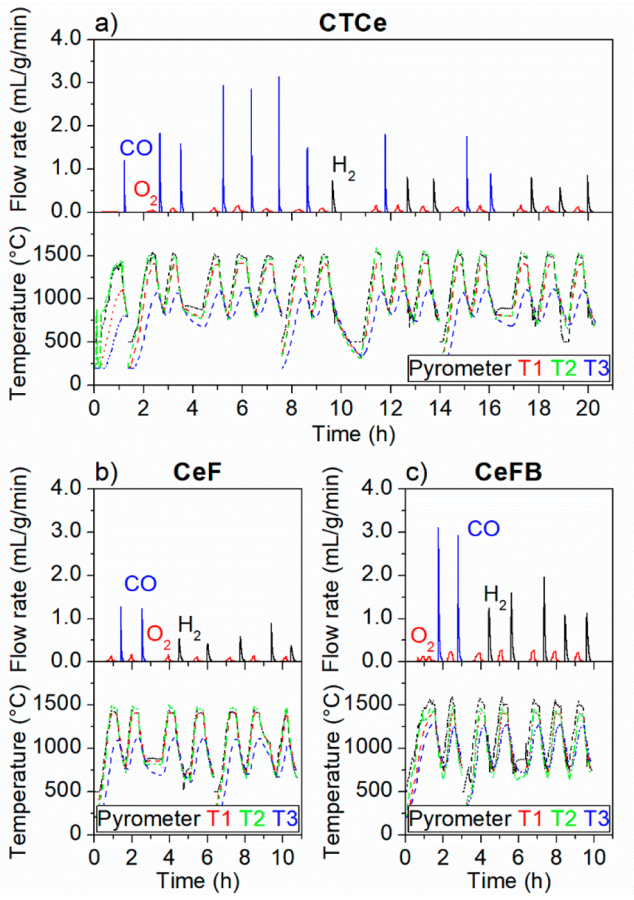

Figure 3. O_2 and fuel production rates during the performed cycles along with the temperature profiles for (a) CTCe (sixteen cycles), (b) CeF (seven cycles), and (c) CeFB (seven cycles). T1, T2, and T3 are the temperatures of the sample interior, sample surface, and the base of the reactor.

temperature gradient measured through the CeFB material in the reactor cavity (150 °C gap between the pyrometer and T1). Although, the reference temperature was maintained at 1400 °C at T1, the part of the reactive material situated above reached a much higher temperature due to the poor thermal conductivity of the fiber boards. Thus, the reactive material situated above T1 achieved a larger reduction extent due to the high temperature reached. The averaged oxygen nonstoichiometry reached by the whole material was thus higher (maximum $\delta \sim 0.055$). In addition, the fiber boards were directly exposed to the high flux solar radiation inside the cavity (no central confiner tube was used for CeFB, as shown in Figure 1), thus increasing dramatically the temperature of the material surface. The superior fuel production performance of CeFB can thus be ascribed to the high reduction temperature reached by the reactive material rather than to the material morphology. Consequently, the O_2 and CO production yields of CeFB were higher than those of CTCe and CeF due to the higher reduction temperature reached by CeFB.

3.1. Materials Performance Comparison. In order to compare the thermochemical performance of the three reactive materials, a reference cycle (characterized by a reduction step at 1400 °C under Ar at atmospheric pressure and an oxidation step with a temperature decrease between 1050 and 850 °C in 25 mol % CO_2) was performed for CTCe (cycle #12), CeF (cycle #1) and CeFB (cycle #1) as presented in Figure 4. The oxygen and fuel production yields were much higher for CeFB than for CeF and CTCe, owing to the different maximum reduction temperature attained by the materials. As the fuel production yield is very sensitive to the reduction extent reached by the reactive material, the O_2 and the CO production yields follow the same trend. For this cycling condition, the highest CO production rate (3.1 mL/g/min) was achieved for CeFB. All the materials present a high reoxidation yield (>87%).

A relevant metric used to evaluate the thermochemical cycle performance is the solar-to-fuel energy conversion efficiency. The instantaneous solar-to-fuel conversion efficiency is defined as follows:

$$\eta_{\text{solar-to-fuel}} = \frac{\dot{n}_{\text{fuel}} \text{HHV}_{\text{fuel}}}{P_{\text{solar}}} \quad (3)$$

where $\dot{n}_{\text{fuel}}$ represents the fuel production rate; HHV_{fuel}, the high heating value of the fuel; and P_{solar}, the solar power input. Furthermore, the cycle efficiency, as defined in eq 4, can also be used to quantify the efficiency related to the actual amount of cycled ceria and to bypass the heat losses inherent to the prototype scale reactor.

$$\eta_{\text{cycle}} = \frac{n_{\text{fuel}} \text{HHV}_{\text{fuel}}}{(\text{Cp}_{\text{CeO}_2} \Delta T + \Delta H(\delta_f)) n_{\text{CeO}_2}} \quad (4)$$

where n_{fuel} represents the fuel production yield in the cycle; Cp_{CeO_2}, the specific heating value of ceria; ΔT, the temperature swing between the reduction and the oxidation steps; $\Delta H(\delta_f)$, the reduction enthalpy for final stoichiometry δ_f; and n_{CeO_2}, the amount of reacting ceria. The reduction enthalpy was calculated as a function of the nonstoichiometry extent

https://dx.doi.org/10.1021/acs.energyfuels.0c01240
Energy Fuels 2020, 34, 9037−9049

Table 3. Operating Parameters along with Oxygen and Fuel Production Amounts for the Three Investigated Reactive Materials

cycle #	T1 reduction step (°C)	pressure (bar)	O_2 produced (μmol/g)	T1 oxidation step (starting−ending temperature; °C)	oxidant gas (oxidant molar fraction)	oxidant flow rate/ total flow rate (L/min)	fuel produced (μmol/g)	peak fuel production rate (mL/g/min)
				CTCe				
1	1107	0.865	25	1040−856	CO_2 (0.25)	0.40/1.60	56	1.2
2	1414	0.871	65	1043−872	CO_2 (0.25)	0.40/1.60	131	1.8
3	1413	0.870	68	1060−887	CO_2 (0.25)	0.40/1.60	122	1.6
4	1405	0.871	75	1056−858	CO_2 (1.00)	2.00/2.00	148	2.9
5	1411	0.110	94	1049−895	CO_2 (0.25)	0.40/1.60	190	2.9
6	1410	0.864	64	949−828	CO_2 (0.25)	0.40/1.60	114	3.1
7	1409	0.871	68	1088−846	CO_2 (0.25)	0.40/1.60	122	1.5
8	1414	0.874	64	1032−830	H_2O (0.18)	0.27/1.47	116	0.7
9	1413	0.870	68	1062−909	CO_2 (0.25)	0.40/1.60	121	1.8
10	1413	0.870	60	1031−834	H_2O (0.18)	0.27/1.47	119	0.8
11	1423	0.913	65	1035−785	H_2O (0.18)	0.27/1.47	129	0.8
12	1410	0.870	68	1054−859	CO_2 (0.25)	0.40/1.60	126	1.8
13	1413	0.871	64	1054−828	CO_2 (0.24)	0.20/0.85	127	0.9
14	1410	0.871	67	1043−782	H_2O (0.39)	0.45/1.15	125	0.8
15	1412	0.905	69	1043−729	H_2O (0.50)	0.45/0.90	122	0.6
16	1405	0.911	64	1049−718	H_2O (0.26)	0.45/1.75	112	0.9
				CeF				
1	1412	0.869	76	1051−840	CO_2 (0.25)	0.40/1.60	131	1.3
2	1413	0.874	71	1055−829	CO_2 (0.25)	0.40/1.60	137	1.2
3	1413	0.871	72	1039−763	H_2O (0.18)	0.27/1.47	129	0.5
4	1411	0.911	66	1041−746	H_2O (0.18)	0.27/1.47	117	0.4
5	1411	0.863	72	1050−716	H_2O (0.39)	0.45/1.15	130	0.6
6	1411	0.909	67	940−702	H_2O (0.18)	0.27/1.47	119	0.9
7	1405	0.901	53	1031−693	H_2O (0.50)	0.45/0.90	101	0.4
				CeFB				
1	1410	0.865	159	1044−776	CO_2 (0.25)	0.40/1.60	302	3.1
2	1417	0.867	146	1046−774	CO_2 (0.25)	0.40/1.60	292	2.9
3	1410	0.869	160	1047−775	H_2O (0.18)	0.27/1.47	288	1.3
4	1413	0.909	146	1039−742	H_2O (0.39)	0.45/1.15	277	1.6
5	1411	0.902	145	960−750	H_2O (0.18)	0.27/1.47	268	2.0
6	1411	0.905	135	1031−757	H_2O (0.18)	0.27/1.47	254	1.1
7	1410	0.906	123	1060−752	H_2O (0.26)	0.45/1.75	230	1.1

according to the procedure described elsewhere.[54] Due to the high fuel production rate, CeFB showed the highest instantaneous solar-to-fuel conversion efficiency (1.5% versus 0.6% and 0.7% for CTCe and CeF, respectively). The low efficiency values are related to the low amount of processed reactive material that induces relatively small CO production yields. Consequently, increasing the reactor scale associated with sensible heat recovery systems should drastically increase the overall efficiency to meet the requirement for an industrial implementation.[55] Regarding the cycle efficiency, CeFB material also achieved the highest value (3.0%) among the tested materials (1.2% for CTCe and 1.3% for CeF). The higher cycle efficiency of CeFB, compared with CTCe and CeF, is attributed to the high reduction extent reached by the reactive material arising from the higher thermal gradient (due to the poor thermal conductivity of this structure and the absence of confiner tube thus changing the heating conditions along the height). The optimization of the solar-to-fuel efficiency is required for a future industrial process implementation as a high efficiency allows decreasing the production cost of the solar fuels.[56]

Table 4 summarizes the total mass of ceria loaded in the reactor and the number of cycles performed during the corresponding continuous on-sun operation along with the total gas amounts produced for the studied reactive materials. Figure 5 plots the oxygen production yields (squares) and the fuel production (bars) depending on the reduction temperature. The cycle performed under low pressure (0.110 bar, cycle #5 for CTCe) during the reduction step is also indicated (hollow square). A low pressure during the reduction step leads to an improvement of both the reduction extent (δ up to 0.032) and the fuel production yield (190 μmol/g), as previously reported.[47,57] In total, the three materials produced 1.92 L of H_2 and 1.40 L of CO, over 16 and 14 cycles, respectively. No significant performance decline with an increasing number of cycles (within the range investigated) was noticeable for CTCe and CeF, which indicates good thermochemical stability and resistance to sintering under the harsh operating solar conditions (though the investigation of long-term stability and performance of such materials during extended on-sun testing periods for hundreds of cycles is still required to provide definite conclusions on suitability for real on-sun operations). In contrast, CeFB showed a strong performance decline with a drop in the fuel production from 302 μmol/g to 230 μmol/g after seven cycles. As stated before, the CeFB material reached a high temperature in its upper part leading to structure densification. The sharp decrease of the fuel production can thus be explained by the densification of

https://dx.doi.org/10.1021/acs.energyfuels.0c01240
Energy Fuels 2020, 34, 9037−9049

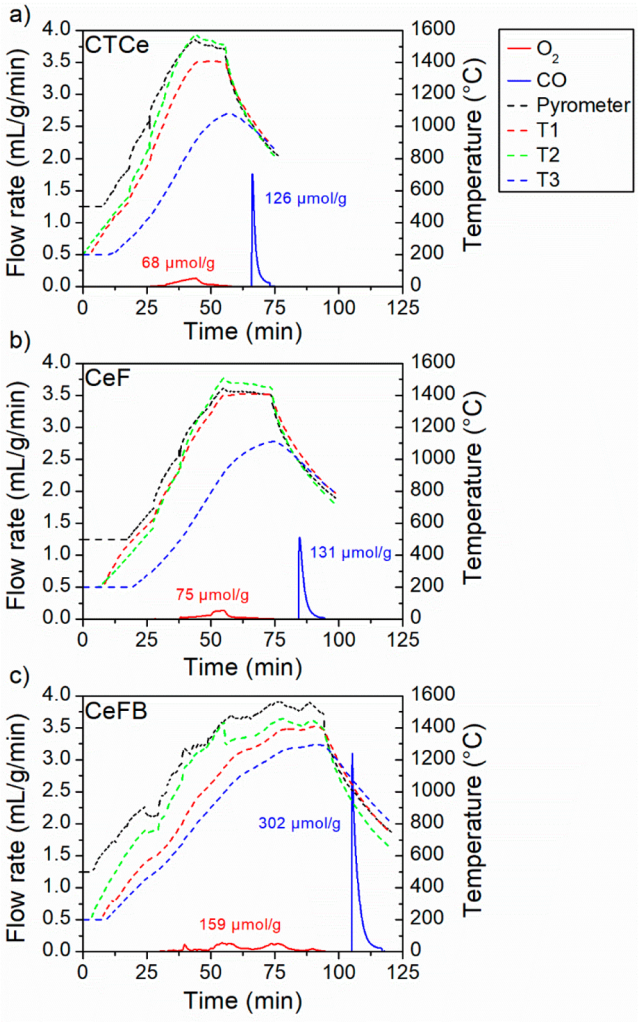

Figure 4. Thermochemical cycles at atmospheric pressure, $T1_{red}$ = 1400 °C and $T1_{ox}$ = 1050−850 °C with 25 mol % CO_2 during the oxidation step for (a) CTCe (cycle #12), (b) CeF (cycle #1), and (c) CeFB (cycle #1).

Table 4. Ceria Mass Loaded in the Reactor, Number of Cycles Associated with Continuous on Sun-Operation Duration along with Total O_2, H_2, and CO Amounts Produced for CTCe, CeF, and CeFB

	CTCe	CeF	CeFB
material mass (g)	25.4096	39.5707	33.321
number of cycle	16	7	7
continuous on sun-operation (h)	20	11	10
total O_2 amount produced (L)	0.50	0.42	0.76
total H_2 amount produced (L)	0.41	0.53	0.98
total CO amount produced (L)	0.72	0.24	0.44

the reactive bulk fiber, which is also due to the thermal gradient arising from low thermal conductivity, and high optical thickness of the material. A similar decrease of the reactivity due to sintering was previously observed with ceria felt.[33] Consequently, ceria fibers do not appear suitable for thermochemical cycles because of their poor thermal stability and low resistance to sintering, despite their ability for fuel production. In addition, the radiative opacity of the fiber bulk might hinder its application when being directly irradiated by solar energy, and therefore, indirect heating may be more favorable.

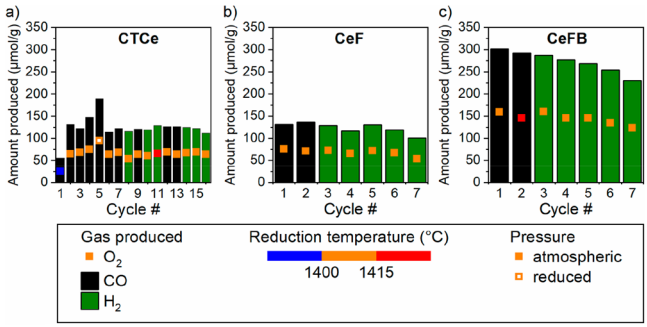

Figure 5. O_2 and fuel production yields over cycles for (a) CTCe, (b) CeF, and (c) CeFB. Squares represent the O_2 production amount, and bars refer to the fuel production. The reduction temperature is indicated by the color of the square.

3.2. Investigation of Operating Parameters. During the oxidation step, a main parameter to be investigated is the oxidation temperature. According to thermodynamics, decreasing the oxidation temperature favors the oxidation reaction. To investigate the impact of the oxidation temperature on the fuel production performance, thermochemical cycles were carried out with a dynamic oxidation temperature regime starting at different oxidation temperatures (~1050 °C and ~950 °C), as represented in Figure 6. Decreasing the starting oxidation temperature by 100 °C leads to the enhancement of the fuel production rate (from 0.5 mL/g/min to 0.9 mL/g/min with H_2O and from 1.8 mL/g/min to 3.1 mL/g/min with CO_2). Furthermore, the necessary duration to reach 90% of the total H_2 amount produced slightly decreased from 8.8 to 7.6 min. The total amounts of H_2 produced are similar, in the range of 119−129 μmol/g. The duration to reach 90% of the total CO amount produced is not really affected (marginal decrease from 2.9 to 2.4 min). Similarly to the H_2 production amounts, the total CO production yields are almost identical in the range of 114−126 μmol/g. A low starting oxidation temperature enhances the fuel production rate, while it does not significantly impact the fuel production yield. Nevertheless, a decrease of the starting oxidation temperature obviously leads to a decrease of the ending oxidation temperature. Thus, the temperature swing between the oxidation and the next reduction step is increased, generating heat losses that can have a negative impact on the global solar-to-fuel efficiency and increasing the global cycle duration.

As the oxidation reaction is chiefly a surface-controlled reaction, the gas flow rates during the oxidation step have also an impact on the fuel production rate. To investigate this effect, the reoxidation step was carried out with two different total gas flow rates at a constant molar fraction of CO_2 (x_{CO_2} = 0.25), as represented in Figure 7. The CO production rate increases with the increase of the total inlet gas flow, reaching 1.76 mL/g/min for a total gas flow rate of 1.60 L/min. In both cases, the CO/CO_2 ratio is similar (the maximal value is around 0.13), which thus does not explain the effect of total inlet gas flow rate. This means that the CO product dilution (higher dilution when increasing the total gas flow rate), along with continuous CO product removal by the carrier gas, favors the oxidation reaction (decreasing the CO partial pressure favors the CO production because the oxidation reaction is shifted to the products side). Moreover, the total CO amount

https://dx.doi.org/10.1021/acs.energyfuels.0c01240
Energy Fuels 2020, 34, 9037−9049

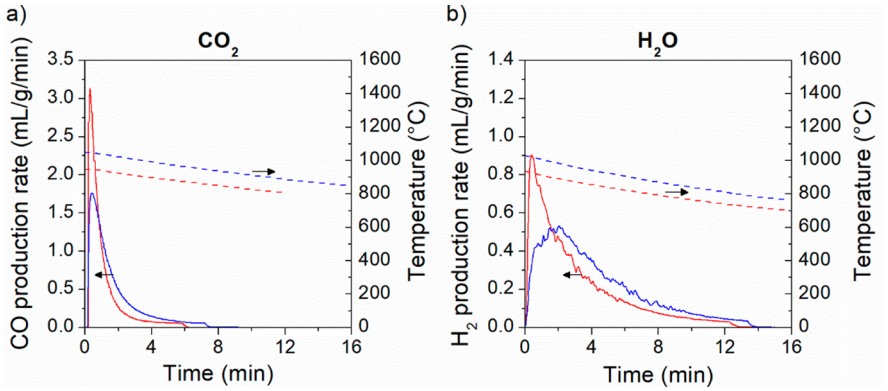

Figure 6. (a) CO production rate from CTCe (solid lines) along with T1 temperature (dashed lines) for 949 °C (cycle #6) and 1054 °C (cycle #12) starting oxidation temperature and (b) H_2 production rate from CeF (solid lines) along with T1 temperature (dashed lines) for 1039 °C (cycle #3) and 940 °C (cycle #6) starting oxidation temperature.

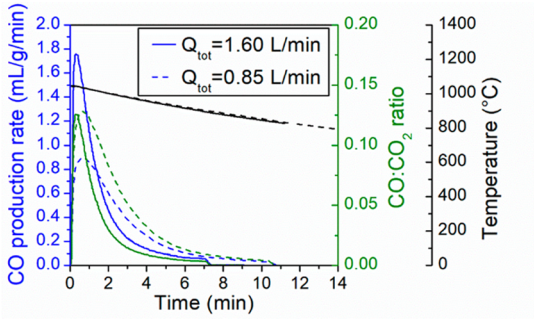

Figure 7. CO production rate from CTCe (blue lines) along with CO/CO_2 ratio (green lines) and T1 temperature (black lines) for different total flow rates during the oxidation step: 1.60 L/min (solid lines, CTCe cycle #12) and 0.85 L/min (dashed lines, CTCe cycle #13) with x_{CO_2} = 0.25.

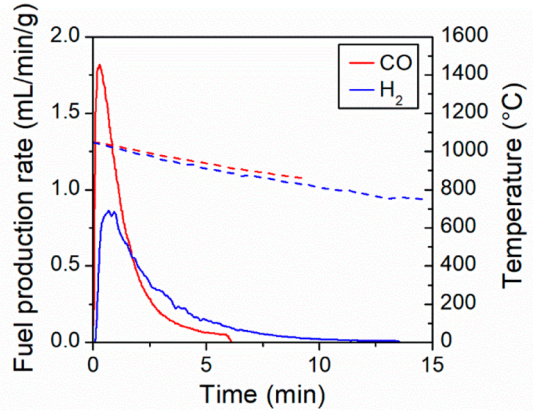

Figure 8. H_2 (cycle #16) and CO (cycle #9) production rates from CTCe (solid lines) along with temperature (dashed lines) with oxidant concentration of 25 mol %

produced is also similar (~126 μmol/g) for both considered total flow rates, in line with the fact that the CO yield is related to δ, which in turn is closely linked to the reduction temperature ($\delta \sim 0.023$ at T1 = 1400 °C). The global CO_2 to CO conversion extent increases with the decrease of the total gas flow rate, because a lower amount of CO_2 is injected during the oxidation step. However, the peak CO_2 to CO conversion is not affected when decreasing the total gas flow rate, because the lower amount of CO_2 used is compensated for by the lower CO production rate. Increasing the total gas flow rate has a beneficial impact on the oxidation reaction, as it promotes mass transfer in the gas phase, which facilitates the access of the oxidant gas to the reactant surface. However, the total gas flow rate should be maintained at reasonable values to avoid useless energy penalties for gas separation and sensible inert gas heating.

The oxidation step was performed with either CO_2 or H_2O as oxidant gas. However, these two gases do not have the same thermodynamic properties. Indeed, thermodynamics indicate a more favorable CO_2 dissociation, due to the higher entropy of the CO_2 dissociation reaction, compared with the H_2O dissociation reaction. In order to investigate the different behavior of the two oxidant gases, Figure 8 presents the fuel production rate evolution with similar oxidation temperatures and oxidant molar fractions, for CO_2 or H_2O as oxidant gas. The peak CO production rate is 2 times higher than the H_2 production rate. Similarly, CO_2 as an oxidant gas shows a beneficial impact on the oxidant conversion extent (2.5%) compared with water (1.0%). Meanwhile, the oxidation step duration to reach 90% of the fuel produced increases from 3.7 min with CO_2 to 6.1 min with H_2O. However, the global H_2 production yield (112 μmol/g) is similar to the CO production yield (121 μmol/g), due to a similar reduction extent ($\delta \sim 0.023$). These results confirm that CO_2 as an oxidant gas enhances the oxidation reaction kinetics. In accordance with the thermodynamic predictions, the CO_2 splitting reaction performed in the solar reactor is more favorable than the water splitting reaction. It is worth pointing out that the reaction kinetics is a key parameter for further industrial implementation, as it globally determines the daily fuel productivity for a solar chemical process. Thus, the oxidation step kinetics should be optimized to reach the fastest fuel production rate. Besides this, hydrogen production presents an advantage in avoiding any further separation step for the oxidant (H_2O can be condensed easily), as opposed to CO production that possibly requires CO/CO_2 separation.

In order to optimize the thermochemical cycle performance, the oxidant molar fraction injected during the oxidation step was investigated. As highlighted before, the total gas flow rate showed a strong impact on the fuel production rate for a constant CO_2 mole fraction. Figure 9 presents the CO production rate with two different inlet CO_2 molar fractions (x_{CO_2}) of 0.25 and 1.00. Increasing x_{CO_2} from 0.25 to 1.00 promotes the CO peak production rate from 1.8 to 2.9 mL/

https://dx.doi.org/10.1021/acs.energyfuels.0c01240
Energy Fuels 2020, 34, 9037−9049

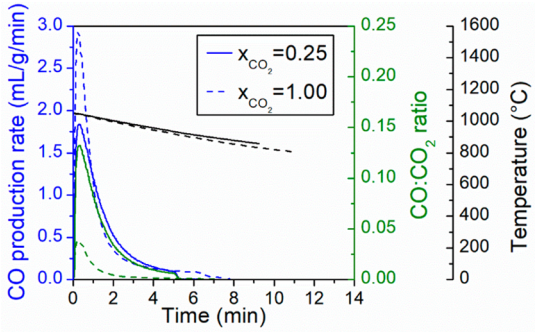

Figure 9. CO production rates from CTCe (blue lines) along with the associated CO/CO_2 ratio (green lines) and T1 temperature (black lines) for a CO_2 molar fraction (x_{CO_2}) of 0.25 (solid lines, cycle #2) and 1.00 (dashed lines, cycle #4).

min/g. This is correlated to the fact that the CO/CO_2 ratio decreased significantly from 0.13 for x_{CO_2} = 0.25 to 0.04 for x_{CO_2} = 1.00 (Figure 9), thus favoring the oxidation reaction toward CO production. A low CO/CO_2 ratio is thermodynamically favorable for the reoxidation reaction, explaining the high CO production rate. This can be explained by a displacement of the reaction equilibrium due to the excess of CO_2 reagent (larger concentration of CO_2 favors the thermodynamic equilibrium toward CO production). Furthermore, the CO yield increased slightly from 132 μmol/g to 148 μmol/g with the greater inlet CO_2 molar fraction. However, the CO_2 to CO conversion extent fell from 2.1% to 0.5% with the increase of x_{CO_2} from 0.25 to 1.00, as well as the peak of CO_2 to CO conversion (from 11.7% to 3.7%). This can be explained by the large excess of CO_2 during the oxidation step when using a high x_{CO_2}, leaving more unreacted CO_2 at the reactor outlet, and thus affecting the CO_2 conversion extent. A low CO_2 to CO conversion extent is unfavorable for an industrial process because of the additional energy required to separate CO from CO_2 in the off-gas.

The impact of inlet CO_2 molar fraction on CO production was thus investigated and unraveled. Regarding water splitting, the impact of the steam molar fraction during the oxidation step on the H_2 production was also studied. Accordingly, the oxidation steps were performed with the following inlet steam concentrations: 18% (1.20 L/min Ar and 0.27 L/min H_2O), 26% (1.30 L/min Ar and 0.45 L/min H_2O), 39% (0.70 L/min Ar and 0.45 L/min H_2O), and 50% (0.45 L/min Ar and 0.45 L/min H_2O), presented in Figure 10a. Unlike CO_2, steam condenses on the cold part at the reactor outlet, making it complicated to evacuate. Thus, the total gas flow rate was not maintained at a constant level to avoid injection of high water amounts. Between 18% and 39%, the H_2 production rates are similar, as well as the H_2 yields (in the range of 112 μmol/g to 129 μmol/g). In contrast, the oxidation step carried out with 50% molar fraction of steam shows a lower peak H_2 production rate (0.56 mL/g/min). However, the H_2 production yield (122 μmol/g) is similar to those obtained with other H_2O molar fractions. A low H_2/H_2O ratio favors the oxidation step according to thermodynamics. On the other hand, the H_2/H_2O ratio decreases with the increase of the H_2O molar fraction, as shown in Figure 10b. Thus, a high H_2O molar fraction should enhance the oxidation step. On the contrary, the highest H_2O molar fraction (50%) presents the lowest H_2 production rate among the considered H_2O molar fractions. This low H_2 production rate can be explained by the total gas flow rate used during the oxidation step (0.90 L/min for 50% H_2O molar fraction compared with 1.15−1.75 L/min for cycles performed with 18% to 39% of H_2O molar fraction). A low total gas flow rate could have hindered the H_2 production rate. As discussed previously in the case of CO_2 splitting, the total gas flow rate has also an influence on the fuel production rate, as it affects the gas product dilution. The low Ar flow rate (0.45 L/min) used with x_{H_2O} = 0.50 leads to a high peak H_2/Ar ratio (0.032) compared with those obtained with x_{H_2O} = 0.39 (0.029), x_{H_2O} = 0.26 (0.017), and x_{H_2O} = 0.18 (0.017). The Ar dilution of produced H_2 is thus much lower when decreasing the Ar flow rate, thereby explaining the lower H_2 production rate. Furthermore, a high carrier gas flow rate favors gas product removal, thus favoring an equilibrium shift toward H_2 production. In addition, the Ar dilution extent of hydrogen can also play a role in the oxidation kinetic, explaining the low H_2 production rate obtained with x_{H_2O} = 0.50. Increasing the H_2O molar fraction without maintaining the total gas flow rate constant does not have any beneficial impact on the fuel production rate nor the fuel production yield.

In summary, a decrease of the pressure during the reduction step results in an increase of the O_2 and fuel production yield. Decreasing the oxidation starting temperature has a beneficial impact on the oxidation step. Moreover, the increase of the total gas flow rate (promoting gas product dilution) during the oxidation step and/or the CO_2 molar fraction (decreasing CO/CO_2 ratio) also leads to an improvement of the oxidation step.

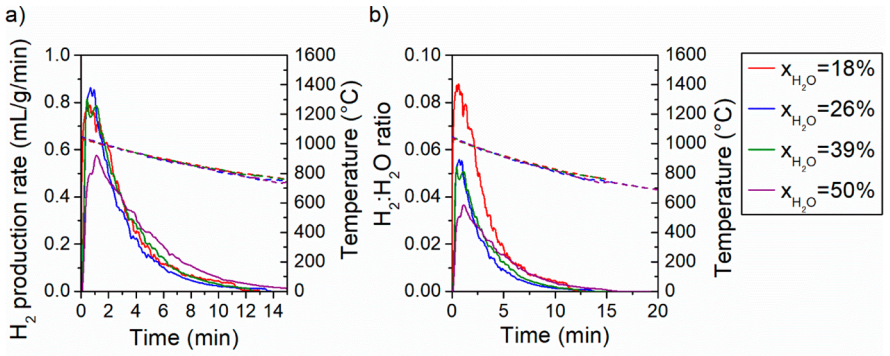

Figure 10. H_2 production (solid lines) along with the temperature (dashed lines) for H_2O molar concentration (x_{H_2O}) of 18% (cycle #11), 26% (cycle #16), 39% (cycle #14), and 50% (cycle #15) for CTCe.

https://dx.doi.org/10.1021/acs.energyfuels.0c01240
Energy Fuels 2020, 34, 9037−9049

3.3. Microstructural Characterization. The morphology of the redox materials that were directly exposed to the high-flux solar irradiation plays a crucial role in their thermochemical performance. Bearing in mind that these materials are cycled at temperatures as high as 1400 °C and subjected to steep temperature gradients, it is of the utmost importance to observe the exposed samples by means of SEM in order to depict any changes in microstructural features, which may result in a loss of performance.

No noticeable changes in morphology were observed for the exposed samples, as shown in Figure 11. The microstructure of

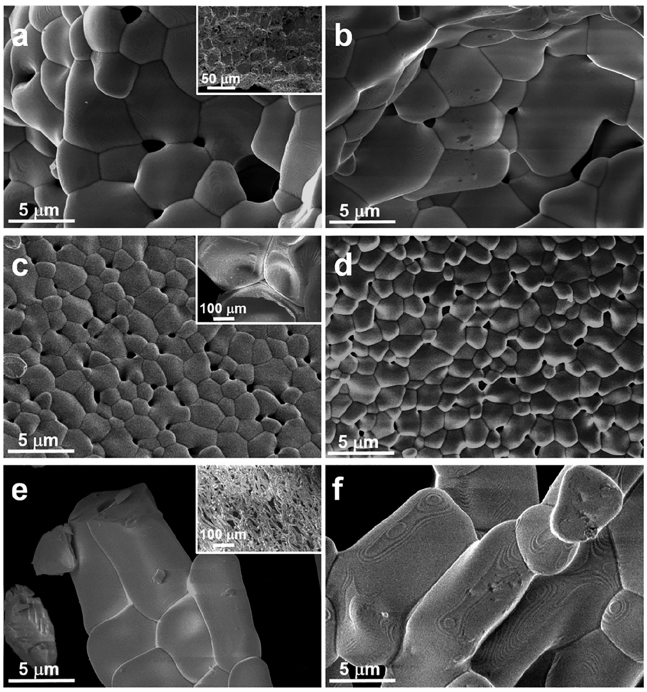

Figure 11. Comparison of representative microscopy images of CTCe, CeF, and CeFB prior (a, c, e) and after (b, d, f) thermal cycling. Insets are images taken at lower magnification.

the CTCe consists of interconnected closed cells with an average size of 25 μm. Residual pores (typically less than 1 μm), located at triple grain joins, remained unchanged after thermal cycling. A similar microstructure was observed for CeF. However, in this case, the morphology consists of macropores with cell sizes of 575 ± 55 μm, some of which have closed cell walls, and hollow struts with thicknesses around 50 ± 5 μm containing micropores. These are typical features of ceramic foams produced by the replication technique.[35] Such macroporous cellular materials (such as foams, fiber mats) are defined as materials possessing high porosity (>70 vol %). Typically, the morphology of the pores is mostly regular and the three-dimensional (3D) architecture of cellular materials derives from the superposition of polyhedral voids (named cells), packed to fill the space efficiently. The CeF grain size (around 2 μm) is slightly smaller than that observed for CTCe owing to the fact that the sintering temperature was only 1450 °C for 30 min, and hence grain growth occurred to a lesser extent than at 1600 °C. These observations are in good agreement with the O_2 and fuel production yield trends recorded. As for CeFB, no evidence of degradation of the fibers could be identified. However, partial shrinkage of the boards after exposure, together with an observed decrease in H_2 yield with increasing numbers of cycles, denotes that densification resulted in a loss of its redox ability for H_2O splitting. The fibers (typically being around 5 μm in diameter) are arranged in a tangled web. The bulk density of CeFB was determined to be 0.89 g cm^{-3}, and consequently, the estimated overall porosity of the fiber boards is 88% (taking into account that the true density of ceria measured by helium pycnometry was 7.65 g cm^{-3}). The bulk density of the CeF material was determined to be 1.03 ± 0.03 g cm^{-3}, which corresponds to a porosity of ~87%. The BET-specific surface area, measured by N_2 adsorption, after thermal cycling, was 0.19 and 0.43 m^2 g^{-1} for CeF and CeFB, respectively. This can also explain the higher hydrogen yields obtained for CeFB compared to their CeF counterparts, in line with the high intrinsic reactivity of ceria fibers despite low thermal stability.[33,49] Basically, the overall higher stability and fuel production rate using CTCe is due to the favorable microstructure obtained from the cork template that favors the solid−gas oxidation reaction, as shown by the material's microstructural characterization.

4. CONCLUSIONS

Different structured ceria materials (biomimetic cork-based ecoceramic, foam and fiber) were tested in a solar reactor to unravel the effect of ceria morphology on thermochemical H_2O and CO_2 splitting performance. The oxygen and the fuel productions were investigated, as well as the thermochemical stability upon two-step redox cycling. The ceria fiber showed the highest reduction extent (averaged oxygen nonstoichiometry up to $\delta \sim 0.055$), thereby leading to superior fuel production yield (above 300 μmol/g in the first cycle, but decreasing in next cycles). This was attributed to the low thermal conductivity of the material and high thermal gradient across its height. It was demonstrated that for these fibers the surface directly irradiated by concentrated sunlight reached much higher temperatures than the target temperature (1400 °C). This was also confirmed by a thermogravimetric analysis, highlighting that O_2 and CO production yields were compliant with the other ceria materials under the same conditions. Furthermore, the fuel yield declined during cycling because of sintering, denoting that this fiber board material is not suitable for achieving stable cycling performance when being directly-irradiated. Noticeably, the cork-templated ceria and the ceria foam showed a good resistance to sintering, with no performance decline over cycles and complete reoxidation (fuel production of about 130 μmol/g, for a reduction step at 1400 °C − atmospheric pressure, yielding $\delta \sim 0.022-0.026$). Finally, the operating parameters were explored with the aim to optimize the fuel production. Increasing the inlet CO_2 molar fraction (from 0.25 to 1.00) or the total gas flow rate during the oxidation step enhanced the fuel production rate, presumably because of the drop of CO/CO_2 ratio or the increase of CO product dilution, both favoring the oxidation reaction toward CO production. Conversely, the steam molar fraction did not significantly have an effect on the H_2 production because the total gas flow rate was not maintained constant and high H_2 dilution by the carrier gas enhanced the H_2 production rate. Moreover, decreasing the starting oxidation temperature led to an enhancement of the fuel production rate (almost double when decreasing the starting oxidation temperature from 1050 to 950 °C). Due to its favorable porous microstructure (mean cell size ~25 μm), the biomimetic cork-based ceria achieved a maximum peak CO

https://dx.doi.org/10.1021/acs.energyfuels.0c01240
Energy Fuels 2020, 34, 9037−9049

production rate of 3.1 mL/min/g after reduction at 1400 °C (at atmospheric pressure), thus outperforming the previously achieved fuel production rates in structured ceria reactors. The fast oxidation rate of this type of material demonstrates its suitability for further studies, while offering the advantages of being cost-attractive and eco-friendly for the green production of solar fuels.

AUTHOR INFORMATION

Corresponding Author

Stéphane Abanades − *Processes, Materials, and Solar Energy Laboratory (PROMES-CNRS), 66120 Font-Romeu, France;* orcid.org/0000-0002-6689-3652; Email: stephane.abanades@promes.cnrs.fr

Authors

Anita Haeussler − *Processes, Materials, and Solar Energy Laboratory (PROMES-CNRS), 66120 Font-Romeu, France*

Fernando A. Costa Oliveira − *LNEG - Laboratório Nacional de Energia e Geologia I.P., LEN - Laboratório de Energia, Materials for Energy Unit, 1649-038 Lisboa, Portugal*

M. Alexandra Barreiros − *LNEG - Laboratório Nacional de Energia e Geologia I.P., LEN - Laboratório de Energia, Materials for Energy Unit, 1649-038 Lisboa, Portugal*

A. P. F. Caetano − *University of Aveiro, Department of Materials and Ceramic Engineering/CICECO − Aveiro Institute of Materials, Campus Universitário de Santiago, 3810-193 Aveiro, Portugal*

Rui M. Novais − *University of Aveiro, Department of Materials and Ceramic Engineering/CICECO − Aveiro Institute of Materials, Campus Universitário de Santiago, 3810-193 Aveiro, Portugal*

Robert C. Pullar − *University of Aveiro, Department of Materials and Ceramic Engineering/CICECO − Aveiro Institute of Materials, Campus Universitário de Santiago, 3810-193 Aveiro, Portugal;* orcid.org/0000-0001-6844-4482

Complete contact information is available at: https://pubs.acs.org/10.1021/acs.energyfuels.0c01240

Notes

The authors declare no competing financial interest.

ACKNOWLEDGMENTS

The experimental setup used in this work was partially funded by the French National Agency for Research (ANR, SUNFUEL project, contract no. ANR-16-CE06-0010). Transnational access to CSP facilities and research infrastructures of CNRS-PROMES through SFERA-III project (grant agreement no. 823802) is also acknowledged. The authors thank R. Garcia (PROMES) for solar reactor design. This work was also supported by Fundação para a Ciência e a Tecnologia (FCT), through the H2CORK project, grant no. PTDC/CTM-ENE/6762/2014 as well as POCI-01-0145-FEDER-016862. R.M.N. was supported by a postdoc research fellowship and FCT grant CEECIND/00335/2017. Thanks are also due to Zircar Zirconia, Inc., Amorim Cork Composites, S.A. and Flexipol − Espumas Sintéticas S.A. for donating the ceria fiber boards, cork samples, and the PU foams, respectively. R.C.P. wishes to thank FCT grant IF/00681/2015 for supporting this work. This work was developed within the scope of the project CICECO−Aveiro Institute of Materials, UIDB/50011/2020 and UIDP/50011/2020, financed by national funds through the FCT/MEC and when appropriate cofinanced by FEDER under the PT2020 Partnership Agreement. The financial support provided by INIESC − National Research Infrastructure for Concentrated Solar Energy through contract ALT20-03-0145-FEDER-022113 is also acknowledged.

REFERENCES

(1) Trainham, J. A.; Newman, J.; Bonino, C. A.; Hoertz, P. G.; Akunuri, N. Whither solar fuels? *Curr. Opin. Chem. Eng.* **2012**, *1*, 204−210.

(2) Graves, C.; Ebbesen, S. D.; Mogensen, M.; Lackner, K. S. Sustainable hydrocarbon fuels by recycling CO_2 and H_2O with renewable or nuclear energy. *Renewable Sustainable Energy Rev.* **2011**, *15*, 1−23.

(3) Lanzafame, P.; Abate, S.; Ampelli, C.; Genovese, C.; Passalacqua, R.; Centi, G.; Perathoner, S. Beyond solar fuels: Renewable energy-driven chemistry. *ChemSusChem* **2017**, *10*, 4409−4419.

(4) Rozzi, E.; Minuto, F. D.; Lanzini, A.; Leone, P. Green synthetic fuels: Renewable routes for the conversion of non-fossil feedstocks into gaseous fuels and their end uses. *Energies* **2020**, *13*, 420.

(5) Takeshita, T.; Yamaji, K. Important roles of Fischer−Tropsch synfuels in the global energy future. *Energy Policy* **2008**, *36*, 2773−2784.

(6) Chueh, W. C.; Haile, S. M. A thermochemical study of ceria: exploiting an old material for new modes of energy conversion and CO_2 mitigation. *Philos. Trans. R. Soc., A* **2010**, *368*, 3269−3294.

(7) Bulfin, B.; Lowe, A. J.; Keogh, K. A.; Murphy, B. E.; Lübben, O.; Krasnikov, S. A.; Shvets, I. V. Analytical model of CeO_2 oxidation and reduction. *J. Phys. Chem. C* **2013**, *117*, 24129−24137.

(8) Ackermann, S.; Scheffe, J. R.; Steinfeld, A. Diffusion of oxygen in ceria at elevated temperatures and its application to H_2O/CO_2 splitting thermochemical redox cycles. *J. Phys. Chem. C* **2014**, *118*, 5216−5225.

(9) Montini, T.; Melchionna, M.; Monai, M.; Fornasiero, P. Fundamentals and catalytic applications of CeO_2 -based materials. *Chem. Rev.* **2016**, *116*, 5987−6041.

(10) Schieber, G. L.; Stechel, E. B.; Ambrosini, A.; Miller, J. E.; Loutzenhiser, P. G. H_2O splitting via a two-step solar thermo-electrolytic cycle based on non-stoichiometric ceria redox reactions: Thermodynamic analysis. *Int. J. Hydrogen Energy* **2017**, *42*, 18785−18793.

(11) Rhodes, N. R.; Bobek, M. M.; Allen, K. M.; Hahn, D. W. Investigation of long term reactive stability of ceria for use in solar thermochemical cycles. *Energy* **2015**, *89*, 924−931.

(12) Bonk, A.; Maier, A.C.; Burnat, D.; Vogt, U.F.; Züttel, A. Investigations on the redox performance of pure and doped CeO_2 by comparing solid state reaction and Pechini synthesis. *Materials for Energy Infrastructure*; Udomkichdecha, W., Mononukul, A., Böllinghaus, T., Lexow, J., Eds.; Springer: Singapore; pp 11−20.

(13) Ackermann, S.; Sauvin, L.; Castiglioni, R.; Rupp, J. L. M.; Scheffe, J. R.; Steinfeld, A. Kinetics of CO_2 reduction over nonstoichiometric ceria. *J. Phys. Chem. C* **2015**, *119*, 16452−16461.

(14) Rager, T. Re-evaluation of the efficiency of a ceria-based thermochemical cycle for solar fuel generation. *Chem. Commun.* **2012**, *48*, 10520−10522.

(15) Call, F.; Roeb, M.; Schmücker, M.; Sattler, C.; Pitz-Paal, R. Ceria doped with zirconium and lanthanide oxides to enhance solar thermochemical production of fuels. *J. Phys. Chem. C* **2015**, *119*, 6929−6938.

(16) Kang, M.; Zhang, J.; Wang, C.; Wang, F.; Zhao, N.; Xiao, F.; Wei, W.; Sun, Y. CO_2 splitting via two step thermochemical reactions over doped ceria/zirconia solid solutions. *RSC Adv.* **2013**, *3*, 18878−18885.

(17) Kang, M.; Wu, X.; Zhang, J.; Zhao, N.; Wei, W.; Sun, Y. Enhanced thermochemical CO_2 splitting over Mg- and Ca-doped ceria/zirconia solid solutions. *RSC Adv.* **2014**, *4*, 5583−5590.

(18) Arifin, D.; Ambrosini, A.; Wilson, S. A.; Mandal, B.; Muhich, C. L.; Weimer, A. W. Investigation of Zr, Gd/Zr, and Pr/Zr − doped

ceria for the redox splitting of water. *Int. J. Hydrogen Energy* **2020**, *45*, 160−174.
(19) Gokon, N.; Suda, T.; Kodama, T. Oxygen and hydrogen productivities and repeatable reactivity of 30-mol%-Fe-, Co-, Ni-, Mn-doped $CeO_{2-\delta}$ for thermochemical two-step water-splitting cycle. *Energy* **2015**, *90*, 1280−1289.
(20) Takacs, M.; Scheffe, J. R.; Steinfeld, A. Oxygen non-stoichiometry and thermodynamic characterization of Zr doped ceria in the 1573−1773 K temperature range. *Phys. Chem. Chem. Phys.* **2015**, *17*, 7813−7822.
(21) Jacot, R.; Naik, J. M.; Moré, R.; Michalsky, R.; Steinfeld, A.; Patzke, G. R. Reactive stability of promising scalable doped ceria materials for thermochemical two-step CO_2 dissociation. *J. Mater. Chem. A* **2018**, *6*, 5807−5816.
(22) Haeussler, A.; Abanades, S.; Jouannaux, J.; Drobek, M.; Ayral, A.; Julbe, A. Recent progress on ceria doping and shaping strategies for solar thermochemical water and CO_2 splitting cycles. *AIMS Mater. Sci.* **2019**, *6*, 657−684.
(23) Dimitrakis, D. A.; Tsongidis, N. I.; Konstandopoulos, A. G. Reduction enthalpy and charge distribution of substituted ferrites and doped ceria for thermochemical water and carbon dioxide splitting with DFT+U. *Phys. Chem. Chem. Phys.* **2016**, *18*, 23587−23595.
(24) Lin, F.; Wokaun, A.; Alxneit, I. Rh-doped ceria: Solar organics from H_2O, CO_2 and sunlight? *Energy Procedia* **2015**, *69*, 1790−1799.
(25) Scheffe, J. R.; Jacot, R.; Patzke, G. R.; Steinfeld, A. Synthesis, characterization, and thermochemical redox performance of Hf^{4+}, Zr^{4+}, and Sc^{3+} doped ceria for splitting CO_2. *J. Phys. Chem. C* **2013**, *117*, 24104−24114.
(26) Bonk, A.; Maier, A. C.; Schlupp, M. V. F.; Burnat, D.; Remhof, A.; Delmelle, R.; Steinfeld, A.; Vogt, U. F. The effect of dopants on the redox performance, microstructure and phase formation of ceria. *J. Power Sources* **2015**, *300*, 261−271.
(27) Andersson, D. A.; Simak, S. I.; Skorodumova, N. V.; Abrikosov, I. A.; Johansson, B. Theoretical study of CeO_2 doped with tetravalent ions. *Phys. Rev. B: Condens. Matter Mater. Phys.* **2007**, *76*, 174119−174129.
(28) Hoes, M.; Muhich, C. L.; Jacot, R.; Patzke, G. R.; Steinfeld, A. Thermodynamics of paired charge-compensating doped ceria with superior redox performance for solar thermochemical splitting of H_2O and CO_2. *J. Mater. Chem. A* **2017**, *5*, 19476−19484.
(29) Call, F.; Roeb, M.; Schmücker, M.; Bru, H.; Curulla-Ferre, D.; Sattler, C.; Pitz-Paal, R. Thermogravimetric analysis of zirconia-doped ceria for thermochemical production of solar fuel. *Am. J. Anal. Chem.* **2013**, *04*, 37−45.
(30) Jacot, R.; Moré, R.; Michalsky, R.; Steinfeld, A.; Patzke, G. R. Trends in the phase stability and thermochemical oxygen exchange of ceria doped with potentially tetravalent metals. *J. Mater. Chem. A* **2017**, *5*, 19901−19913.
(31) Ramos-Fernandez, E. V.; Shiju, N. R.; Rothenberg, G. Understanding the solar-driven reduction of CO_2 on doped ceria. *RSC Adv.* **2014**, *4*, 16456−16463.
(32) Pullar, R.; Novais, R.; Caetano, A.; Barreiros, M. A.; Abanades, S.; Oliveira, F. A. C. A review of solar thermochemical CO_2 splitting using ceria-based ceramics with designed morphologies and microstructures. *Front. Chem.* **2019**, *7*, 601.
(33) Furler, P.; Scheffe, J. R.; Steinfeld, A. Syngas production by simultaneous splitting of H_2O and CO_2 via ceria redox reactions in a high-temperature solar reactor. *Energy Environ. Sci.* **2012**, *5*, 6098−6103.
(34) Schwartzwalder, K.; Somers, A. V. Method of making porous ceramic articles. U.S. Patent US3090094A, May 21, 1963.
(35) Furler, P.; Scheffe, J.; Gorbar, M.; Moes, L.; Vogt, U.; Steinfeld, A. Solar thermochemical CO_2 splitting utilizing a reticulated porous ceria redox system. *Energy Fuels* **2012**, *26*, 7051−7059.
(36) Furler, P.; Scheffe, J.; Marxer, D.; Gorbar, M.; Bonk, A.; Vogt, U.; Steinfeld, A. Thermochemical CO_2 splitting *via* redox cycling of ceria reticulated foam structures with dual-scale porosities. *Phys. Chem. Chem. Phys.* **2014**, *16*, 10503−10511.
(37) Venstrom, L. J.; Petkovich, N.; Rudisill, S.; Stein, A.; Davidson, J. H. The effects of morphology on the oxidation of ceria by water and carbon dioxide. *J. Sol. Energy Eng.* **2012**, *134*, 011005−011012.
(38) Venstrom, L. J.; Petkovich, N.; Rudisill, S.; Stein, A.; Davidson, J. H. The oxidation of macroporous cerium and cerium-zirconium oxide for the solar thermochemical production of fuels. In *ASME 2011 5th International Conference on Energy Sustainability, Parts A, B, and C*; ASMEDC: Washington, DC; pp 1585−1593.
(39) Petkovich, N. D.; Rudisill, S. G.; Venstrom, L. J.; Boman, D. B.; Davidson, J. H.; Stein, A. Control of heterogeneity in nanostructured $Ce_{1-x}Zr_xO_2$ binary oxides for enhanced thermal stability and water splitting activity. *J. Phys. Chem. C* **2011**, *115*, 21022−21033.
(40) Malonzo, C. D.; De Smith, R. M.; Rudisill, S. G.; Petkovich, N. D.; Davidson, J. H.; Stein, A. Wood-templated CeO_2 as active material for thermochemical CO production. *J. Phys. Chem. C* **2014**, *118*, 26172−26181.
(41) Costa Oliveira, F. A.; Barreiros, M. A.; Abanades, S.; Caetano, A. P. F.; Novais, R. M.; Pullar, R. C. Solar thermochemical CO_2 splitting using cork-templated ceria ecoceramics. *J. CO_2 Util.* **2018**, *26*, 552−563.
(42) Singh, M. Environmentally conscious ceramics (ecoceramics) from natural wood precursors. *Curr. Opin. Solid State Mater. Sci.* **2003**, *7*, 247−254.
(43) Costa Oliveira, F. A.; Barreiros, M. A.; Haeussler, A.; Caetano, A.; Mouquinho, A. I.; Oliveira e Silva, P. M.; Novais, R. M.; Pullar, R. C.; Abanades, S. High performance cork-templated ceria for solar thermochemical hydrogen production via two-step water-splitting cycles. *Sustainable Energy Fuels* **2020**, *4*, 3077−3089.
(44) Chueh, W. C.; Falter, C.; Abbott, M.; Scipio, D.; Furler, P.; Haile, S. M.; Steinfeld, A. High-flux solar-driven thermochemical dissociation of CO_2 and H_2O using nonstoichiometric ceria. *Science* **2010**, *330*, 1797−1801.
(45) Cho, H. S.; Myojin, T.; Kawakami, S.; Gokon, N.; Kodama, T.; Kang, Y. H.; Lee, S. N.; Chai, K. K.; Yoon, H. K.; Lee, H. J. Solar demonstration of thermochemical two-step water splitting cycle using CeO_2/MPSZ ceramic foam device by $45kW_{th}$ KIER solar furnace. *Energy Procedia* **2014**, *49*, 1922−1931.
(46) Marxer, D.; Furler, P.; Takacs, M.; Steinfeld, A. Solar thermochemical splitting of CO_2 into separate streams of CO and O_2 with high selectivity, stability, conversion, and efficiency. *Energy Environ. Sci.* **2017**, *10*, 1142−1149.
(47) Haeussler, A.; Abanades, S.; Julbe, A.; Jouannaux, J.; Drobek, M.; Ayral, A.; Cartoixa, B. Remarkable performance of microstructured ceria foams for thermochemical splitting of H_2O and CO_2 in a novel high-temperature solar reactor. *Chem. Eng. Res. Des.* **2020**, *156*, 311−323.
(48) Haeussler, A.; Abanades, S.; Julbe, A.; Jouannaux, J.; Cartoixa, B. Solar thermochemical fuel production from H_2O and CO_2 splitting via two-step redox cycling of reticulated porous ceria structures integrated in a monolithic cavity-type reactor. *Energy* **2020**, *201*, 117649.
(49) Gladen, A. C.; Davidson, J. H. The morphological stability and fuel production of commercial fibrous ceria particles for solar thermochemical redox cycling. *Sol. Energy* **2016**, *139*, 524−532.
(50) Novais, R. M.; Pullar, R. C. Comparison of low and high pressure infiltration regimes on the density and highly porous microstructure of ceria ecoceramics made from sustainable cork templates. *J. Eur. Ceram. Soc.* **2019**, *39*, 1287−1296.
(51) Abanades, S.; Legal, A.; Cordier, A.; Peraudeau, G.; Flamant, G.; Julbe, A. Investigation of reactive cerium-based oxides for H_2 production by thermochemical two-step water-splitting. *J. Mater. Sci.* **2010**, *45*, 4163−4173.
(52) Marxer, D.; Furler, P.; Scheffe, J.; Geerlings, H.; Falter, C.; Batteiger, V.; Sizmann, A.; Steinfeld, A. Demonstration of the entire production chain to renewable kerosene via solar thermochemical splitting of H_2O and CO_2. *Energy Fuels* **2015**, *29*, 3241−3250.
(53) Furler, P.; Marxer, D.; Takacs, M.; Steinfeld, A. Solar thermochemical reactor technology for splitting CO_2. *AIP Conf. Proc.* **2017**, *2033*, 130005.

https://dx.doi.org/10.1021/acs.energyfuels.0c01240
Energy Fuels 2020, 34, 9037−9049

(54) Panlener, R. J.; Blumenthal, R. N.; Garnier, J. E. A thermodynamic study of nonstoichiometric cerium dioxide. *J. Phys. Chem. Solids* **1975**, *36*, 1213−1222.
(55) Siegel, N. P.; Miller, J. E.; Ermanoski, I.; Diver, R. B.; Stechel, E. B. Factors affecting the efficiency of solar driven metal oxide thermochemical cycles. *Ind. Eng. Chem. Res.* **2013**, *52*, 3276−3286.
(56) Falter, C.; Scharfenberg, N.; Habersetzer, A. Geographical potential of solar thermochemical jet fuel production. *Energies* **2020**, *13*, 802.
(57) Scheffe, J. R.; Steinfeld, A. Thermodynamic analysis of cerium-based oxides for solar thermochemical fuel production. *Energy Fuels* **2012**, *26*, 1928−1936.

https://dx.doi.org/10.1021/acs.energyfuels.0c01240
Energy Fuels 2020, 34, 9037−9049